Supporting Information

A 2D MoS_2-Based Active-Matrix Photosensor Array for Neuromorphic Vision

Yitong Chen, Rui Wang, Siyu Zhang, Feilin Chen, Yingjie Tang, Shuhui Ren, Dingwei Li, Yan Wang, Huihui Ren, Guolei Liu, Fanfan Li, Hong Wang, Bowen Zhu**

Emails: hongwang@xidian.edu.cn; zhubowen@westlake.edu.cn

Keywords: 2D materials, active-matrix array, neuromorphic vision, visual processing

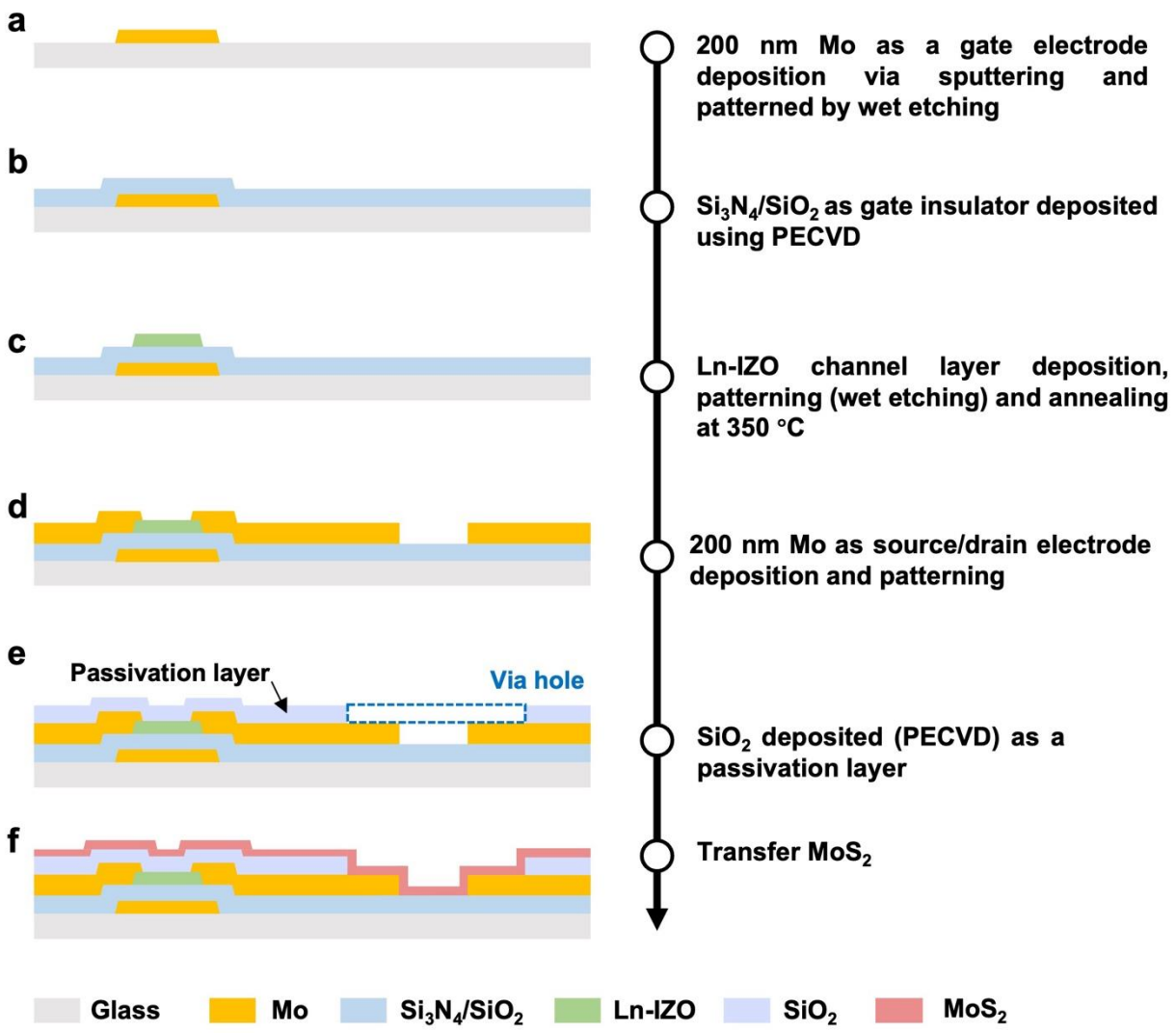

Figure S1. Schematic diagram of the fabrication process of the active-matrix photosensor array (AM-PA).

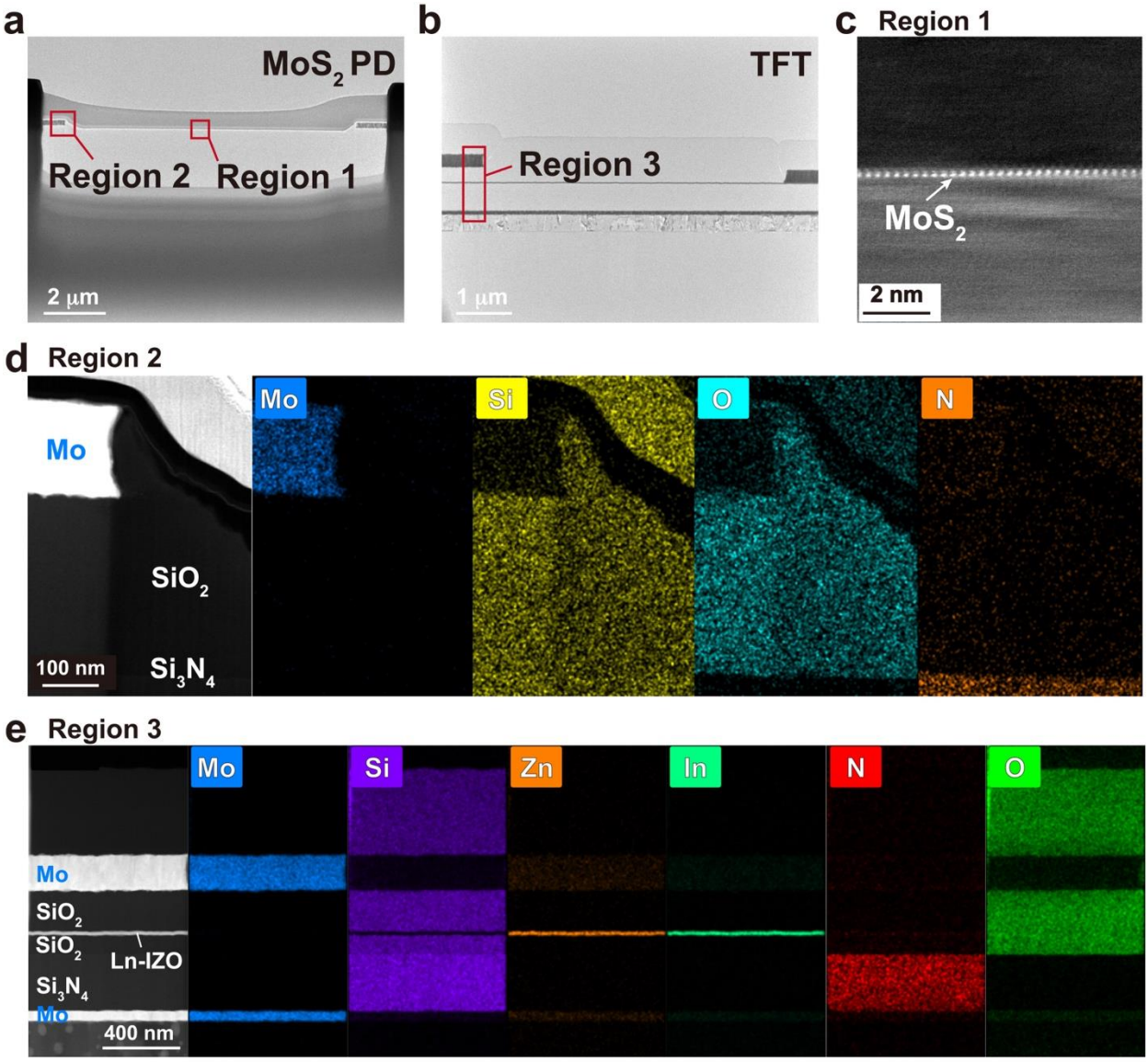

Figure S2. (a-b) Cross-sectional transmission electron microscopy (TEM) images of the MoS_2 PD and Ln-IZO TFT. (c) The enlarged region 1 of the MoS_2 PD, showing a monolayer MoS_2. (d) The enlarged region 2 of the MoS_2 PD with the corresponding chemical distribution of elements molybdenum (Mo), silicon (Si), oxygen (O), and nitrogen (N). (e) The enlarged region 3 of the Ln-IZO TFT, and the corresponding elemental mapping of molybdenum (Mo), silicon (Si), zinc (Zn), indium (In), and nitrogen (N), oxygen (O).

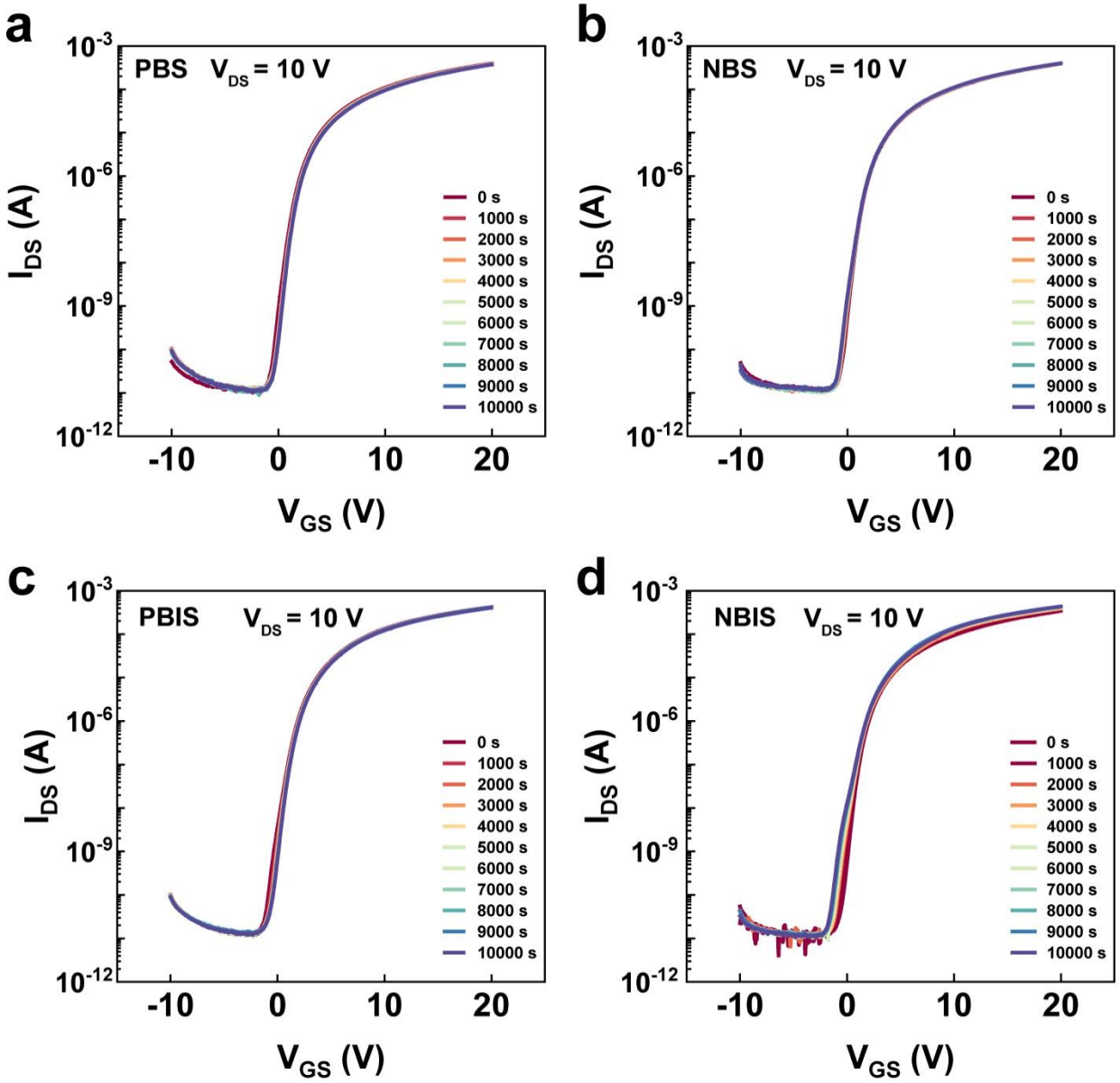

Figure S3. Stability tests of the Ln-IZO TFT. (a-b) Time-dependent transfer curve variations of the Ln-IZO TFT under (a) positive bias stress (PBS) and (b) negative bias stress (NBS) tests. (c-d) Time-dependent transfer curve variations of the Ln-IZO TFT under (c) positive bias illumination stress (PBIS) and (d) negative bias illumination stress (NBIS) tests. In all tests, V_{GS} sweeps from -10 to 20 V in 0.05 V/step, with V_{DS} value keeps in 0.1 V. The PBS and PBIS tests were performed with V_{GS} of +20 V, while NBS and NBIS tests were conducted with V_{GS} of -20 V. The PBIS and NBIS tests were combined with white LED light illumination at 5 mW/cm^2.

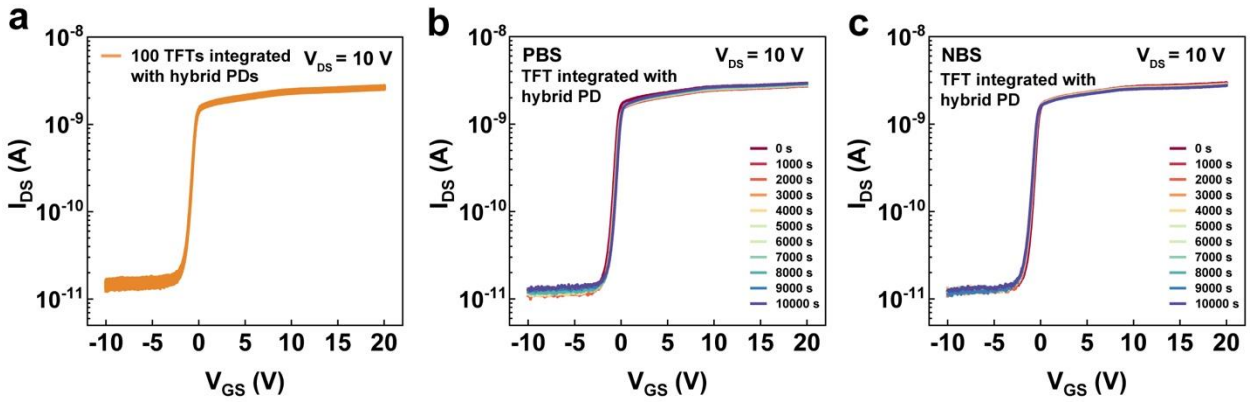

Figure S4. (a) Transfer curves for 100 switching TFTs after integration with the hybrid MoS_2 PDs. (b-c) Time-dependent transfer curve variations of the 1T-1PD under (c) PBS and (d) NBS tests. In all tests, V_{GS} sweeps from -10 to 20 V in 0.05 V/step, with V_{DS} value keeps in 0.1 V. The PBS tests were performed with gate bias of +20 V, while NBS tests were conducted with gate bias of -20 V. Upon integrating the MoS_2 PD with the TFT, the overall current in the on-state becomes smaller compared to the standalone TFT. This difference arises because the MoS_2 PD adds a series resistance that constrains the total current flow.

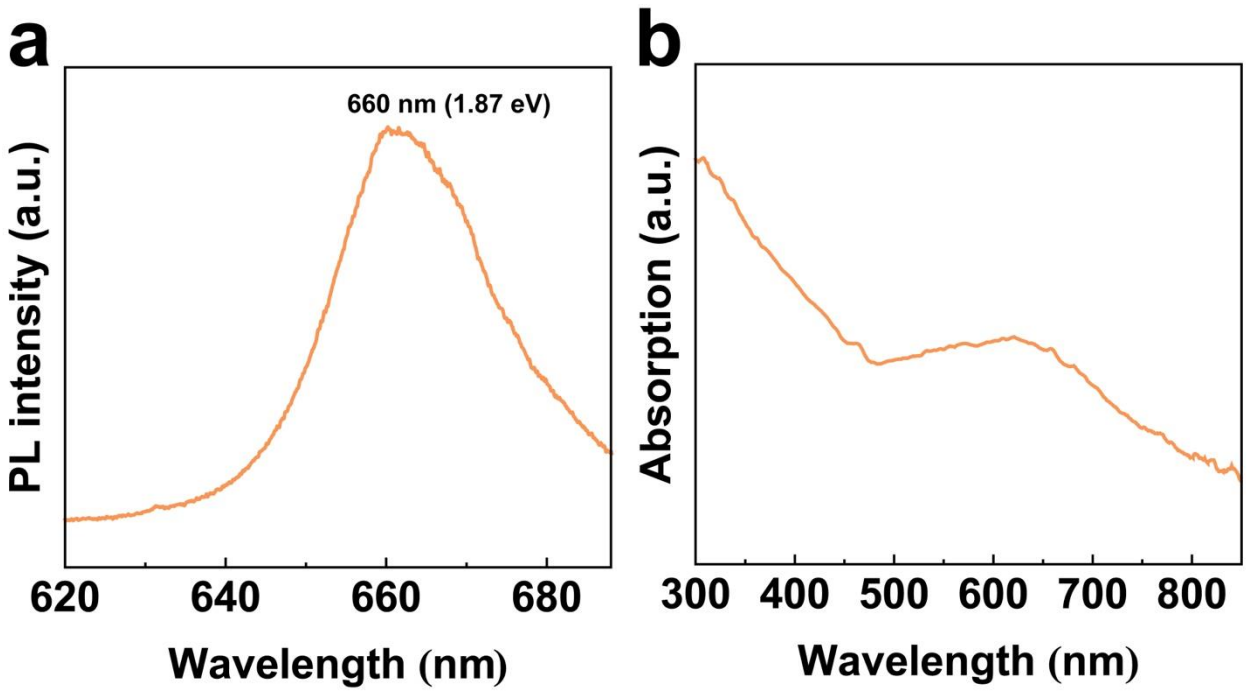

Figure S5. Photoluminescence (PL) (a) and absorbance (b) spectra of monolayer MoS_2.

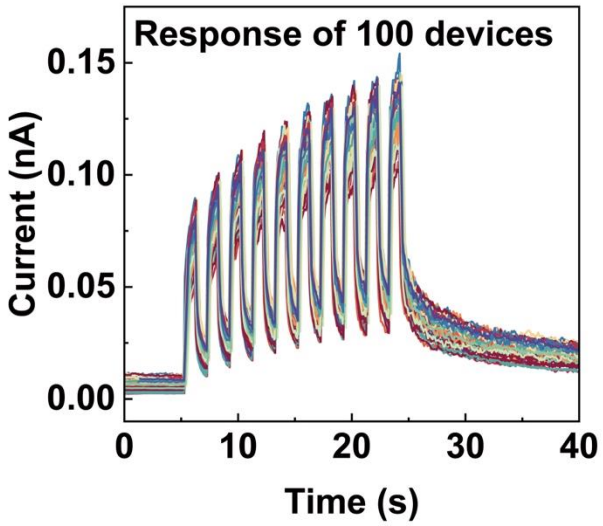

Figure S6. The optoelectronic performance of 100 MoS_2 PDs in the array. The photocurrent was measured as a function of time under optical pulse stimulation. (650 nm, 0.2 μW/cm^2 at 0.5 Hz, V_{DS} = 0.1 V).

Figure S7. The detailed optoelectronic performance of 100 MoS_2 PDs in the array. The photocurrent was measured as a function of time under optical pulse stimulation. (650 nm, 0.2 μW/cm^2 at 0.5 Hz, V_{DS} = 0.1 V).

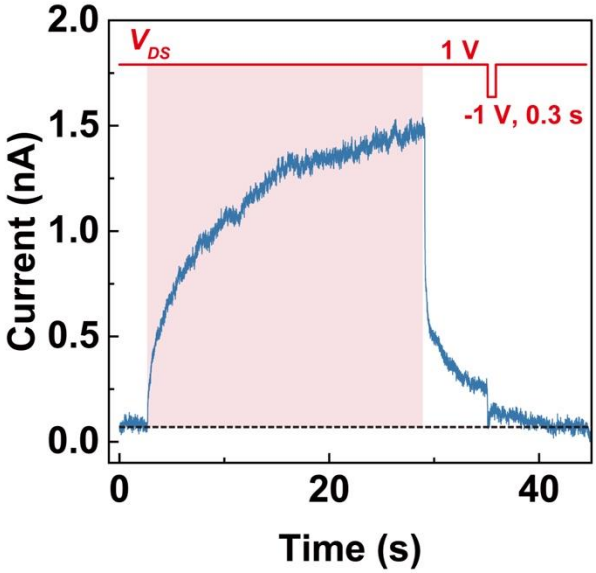

Figure S8. The reset operation after optical stimulation. The photocurrent response to an optical pulse. The optical pulse was 650 nm with an intensity of 10 μW/cm^2 at 0.5 Hz, V_{DS} = 1 V. After the optical pulse, we set the data line (V_{DS}) to -1 V for 0.3 s, after which we read the current at V_{DS} = 1 V. The stored signals can be reset by setting the data line (V_{DS}) to -1 V for 0.3 s, after which we read the current at V_{DS} = 1 V. During this interval, the photogenerated charges responsible for PPC are discharged, effectively erasing the previously stored signal. Any additional energy consumption introduced by this external reset step can be estimated using $E = |I_{peak} \times V \times t|$, where I_{peak} is the peak current, V is the applied V_{DS} voltage, and t is the reset duration. Under our operation conditions (voltage is about 1 V, I_{peak} is about 2.38×10^{-11}, t = 0.3 s), the total energy required for the reset is approximately 7.14 pJ.

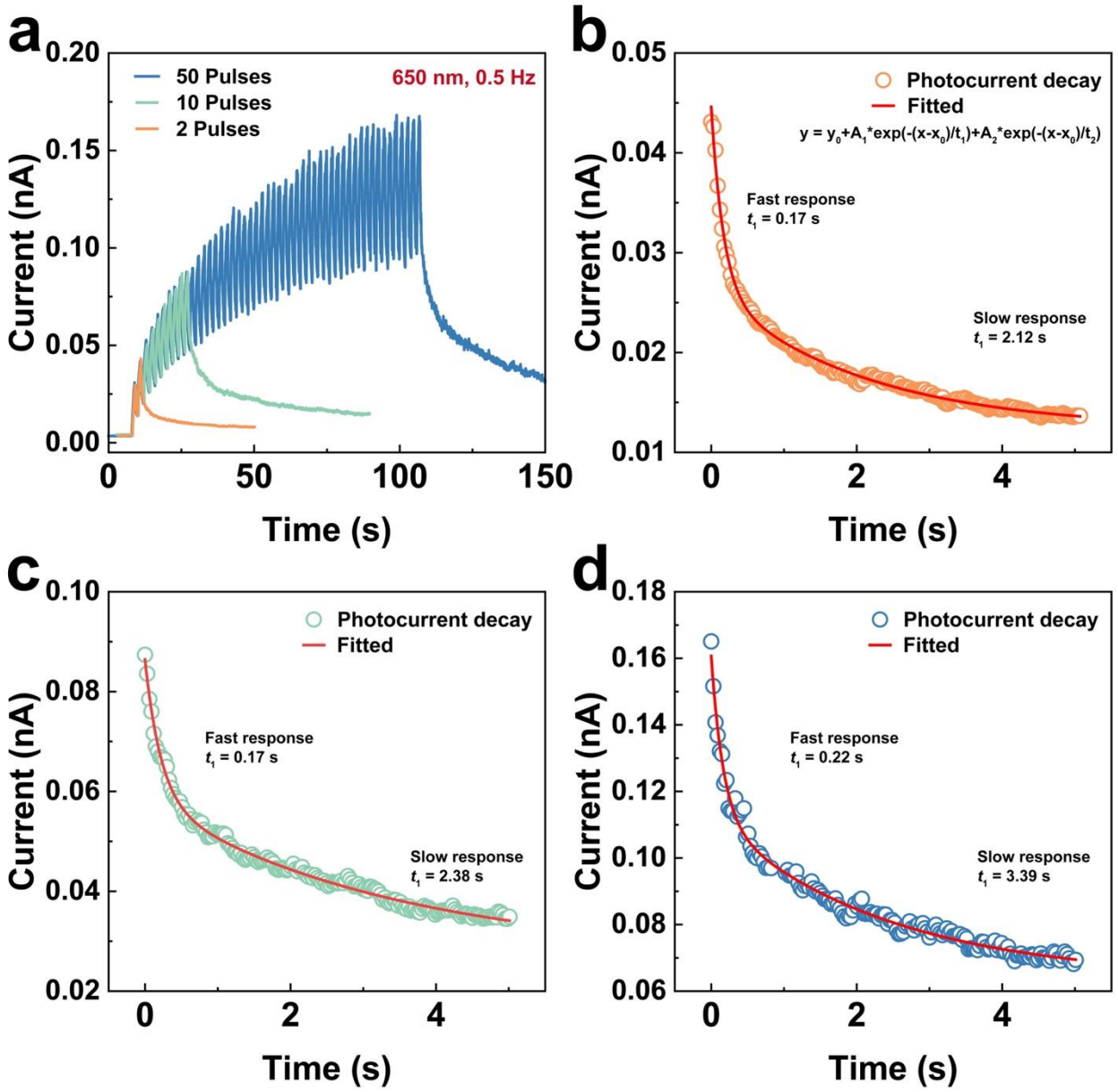

Figure S9. Optical-stimulated sensitive characteristics at 650 nm (red). (a) The photocurrent was measured as a function of time under varying optical pulse stimulations. The applied optical pulse was 650 nm with an intensity of 0.2 μW/cm² at 0.5 Hz, while the voltage applied between the drain and source (V_{DS}) was 0.1 V. (b-d) The photocurrent decay following pulse stimulation was fitted using a double exponential decay function, indicating both fast and slow decay mechanisms. The fast decay corresponds to an intrinsic photoconduction mechanism, while the slow decay is attributed to slow trap states. As optical intensity increases, more photogenerated carriers are produced, resulting in higher current levels. Simultaneously, a greater number of traps are filled, leading to a more pronounced slow decay. (b) The decay curve after two optical pulses, extracted from (a). (c) The decay curve after ten optical pulses. (d) The decay curve after fifty optical pulses, both extracted from (a).

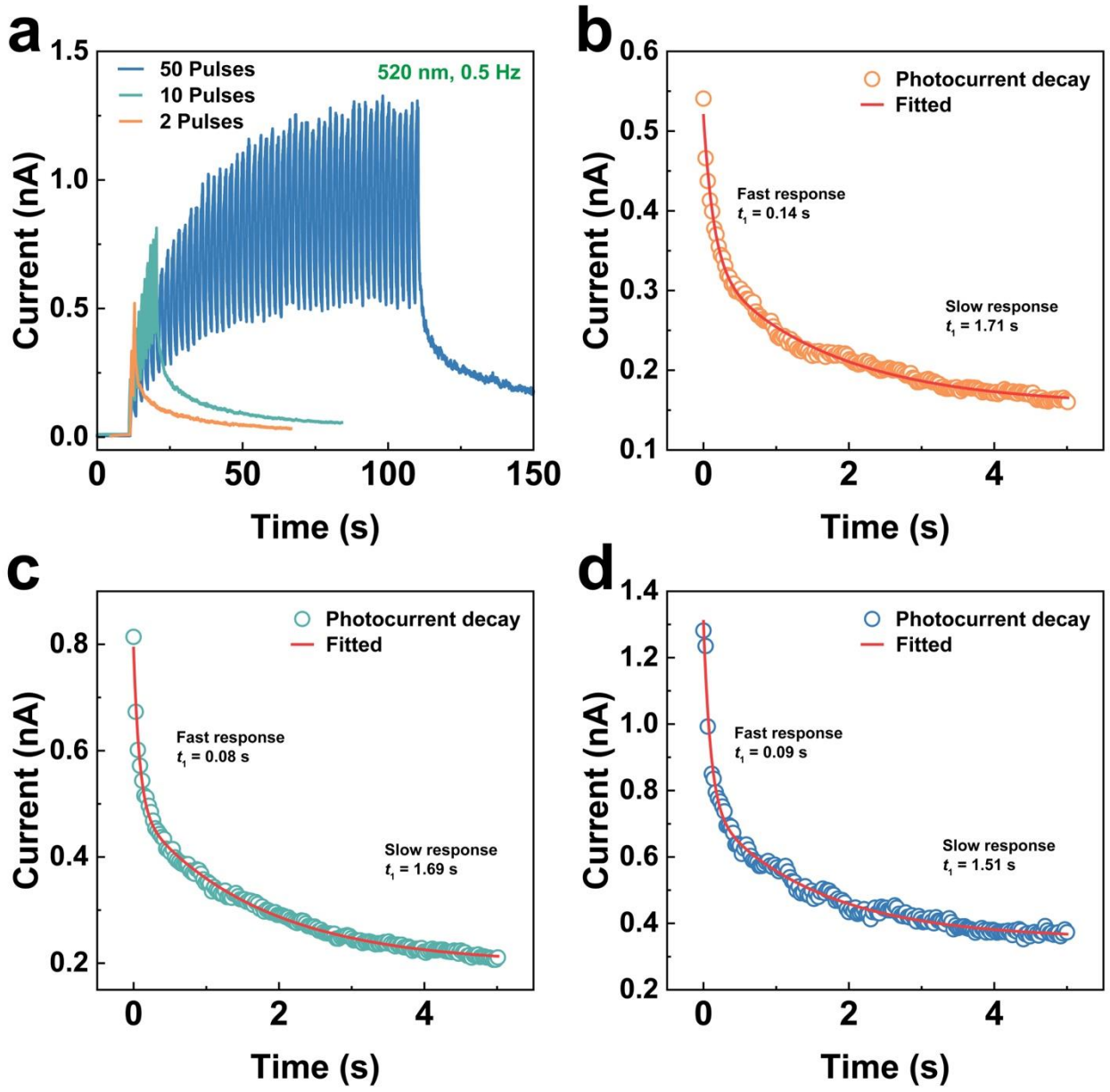

Figure S10. Optical-stimulated sensitive characteristics at 520 nm (green). (a) The photocurrent was measured as a function of time under varying optical pulse stimulations. The applied optical pulse was 520 nm with an intensity of 0.2 μW/cm² at 0.5 Hz, while the voltage applied between the drain and source (V_{DS}) was 0.1 V. (b) The decay curve after two optical pulses, extracted from (a). (c) The decay curve after ten optical pulses. (d) The decay curve after fifty optical pulses, both extracted from (a).

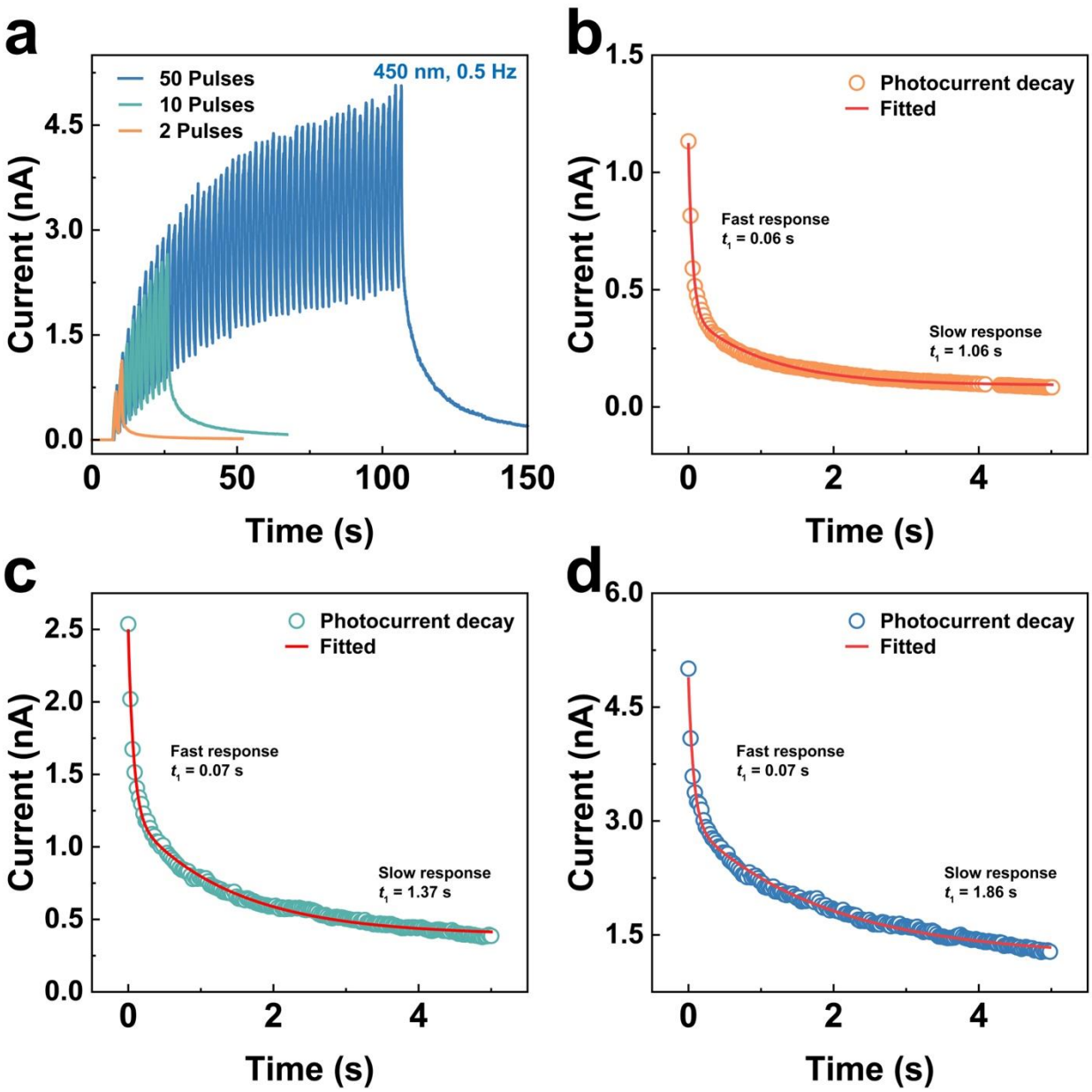

Figure S11. Optical-stimulated sensitive characteristics at 450 nm (blue). (a) The photocurrent was measured as a function of time under varying optical pulse stimulations. The applied optical pulse was 450 nm with an intensity of 0.2 μW/cm² at 0.5 Hz, while the voltage applied between the drain and source (V_{DS}) was 0.1 V. (b) The decay curve after two optical pulses, extracted from (a). (c) The decay curve after ten optical pulses. (d) The decay curve after fifty optical pulses, both extracted from (a).

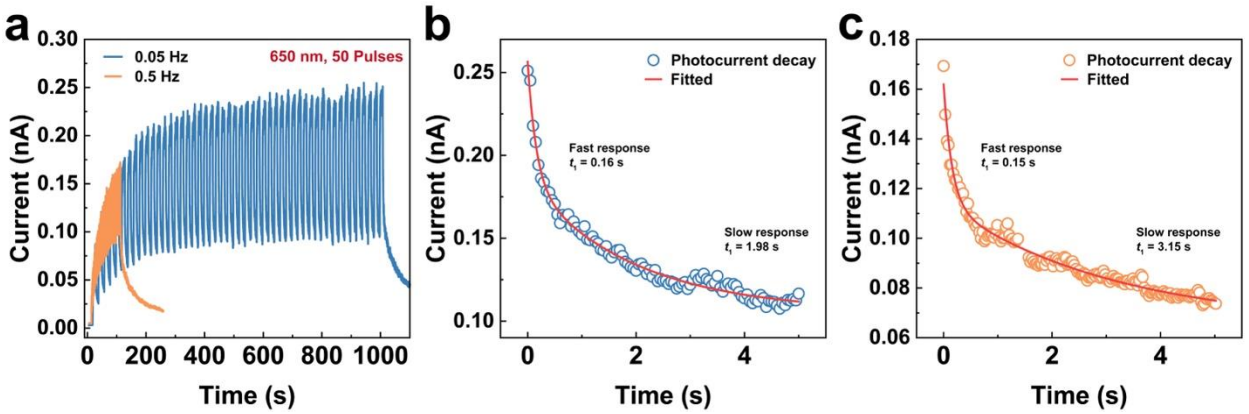

Figure S12. Optical-stimulated sensitive characteristics under different pulse frequencies. (a) The photocurrent was measured as a function of time under varying optical pulse frequency stimulations. (b) The decay curve after optical pulses with an intensity of 0.8 μW/cm² at 0.05 Hz, extracted from (a). (c) The decay curve after optical pulses with an intensity of 0.8 μW/cm² at 0.5 Hz, extracted from (a).

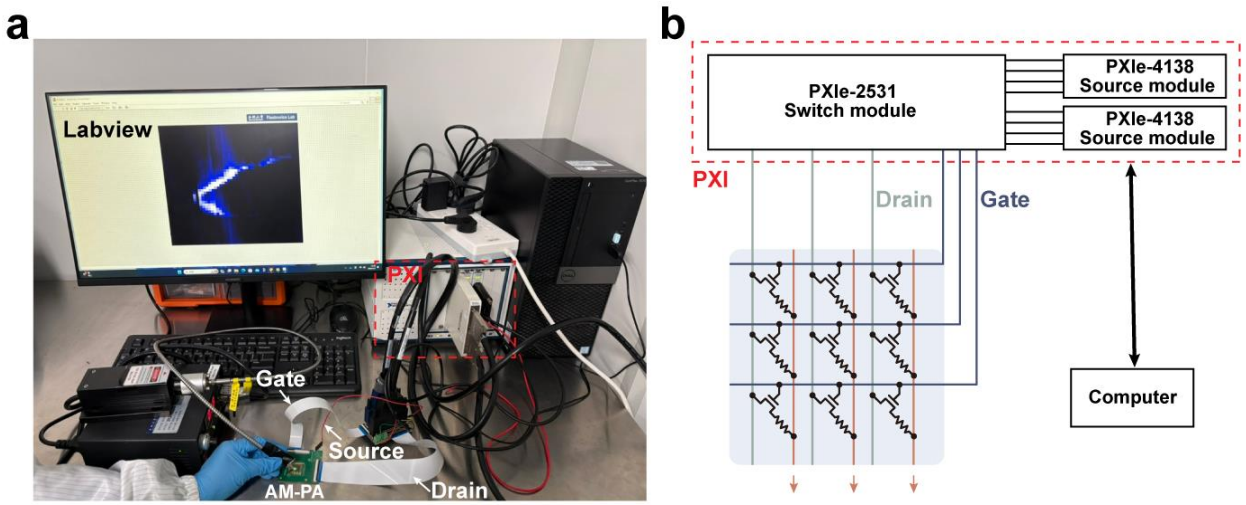

Figure S13. (a) Experimental setup of AM-PA for static image sensing and in-array visual spatiotemporal processing. (b) Overall schematic of multiplexing using PXI system with LabVIEW program. For static image preprocessing, a stainless-steel mask (2 mm thick) with a cut-out "W" pattern was placed on the AM-PA, and the array was illuminated with 520 nm light. The resulting pixel-level measurements, which capture the static image pre-processing capabilities, are depicted in Figures 3g-h. The dynamic vision processing was evaluated by exploiting the light-tunable conductance and residual photocurrent characteristics of the MoS_2 PDs. The time-dependent photocurrent decay, observed at the array level, enabled the reconstruction of a moving light source's trajectory and direction, as illustrated in Figure 4.

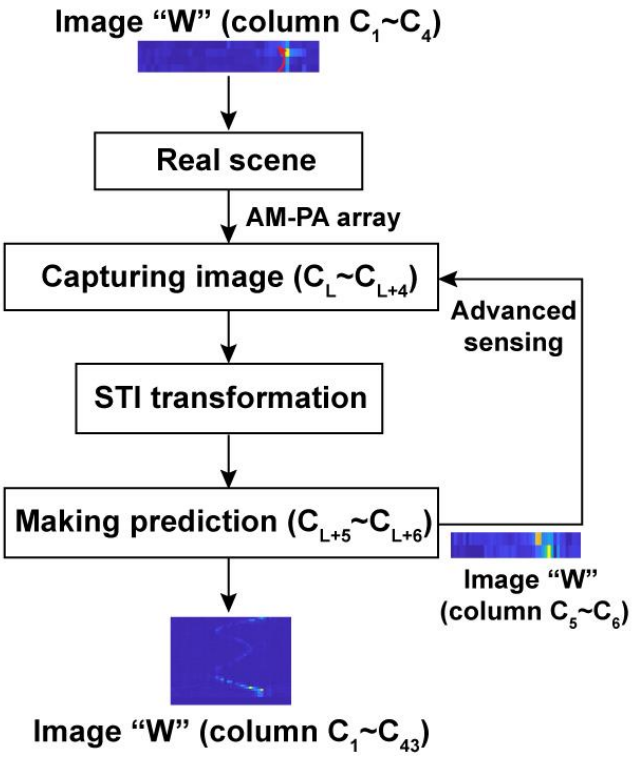

Figure S14. The flow chart for predicting dynamic visual inputs.

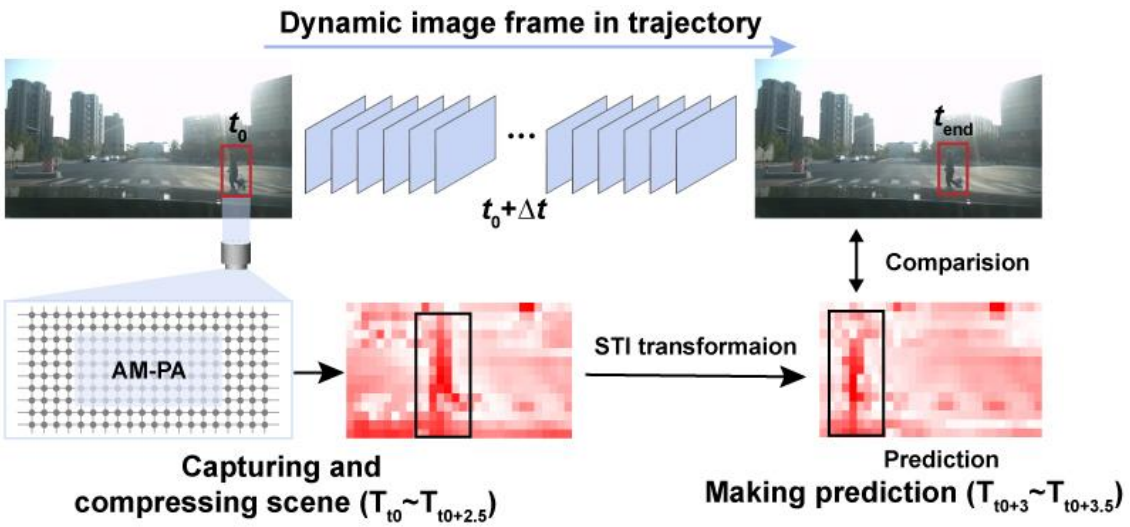

Figure S15. The flow chart for predicting motion trajectory.

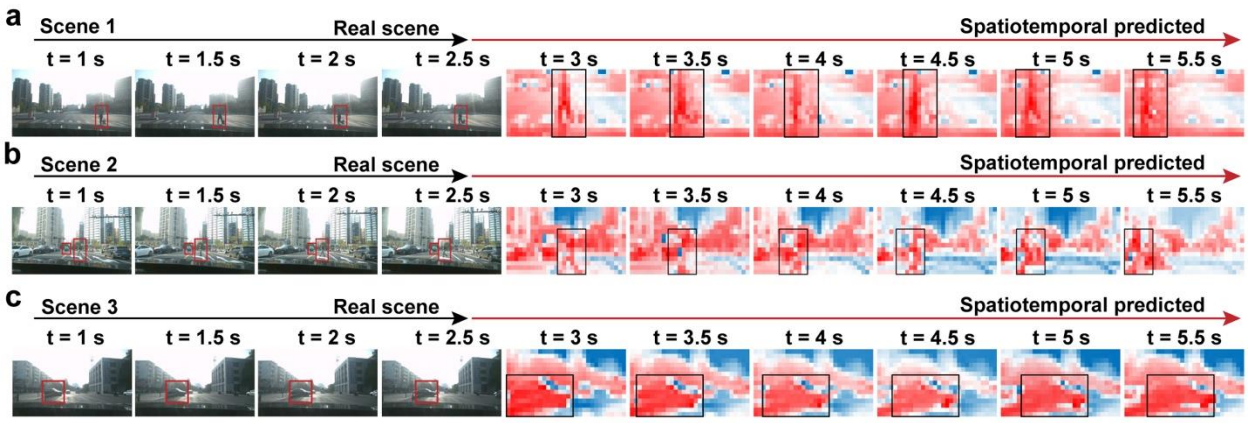

Figure S16. The real scene and prediction results based on AM-PA array. Sequential image frames recorded over time (from t_0 to t_{end}) are used to extract motion trajectories. The first few frames are employed to predict subsequent frames, and the predicted results are compared with actual scene data to evaluate accuracy.

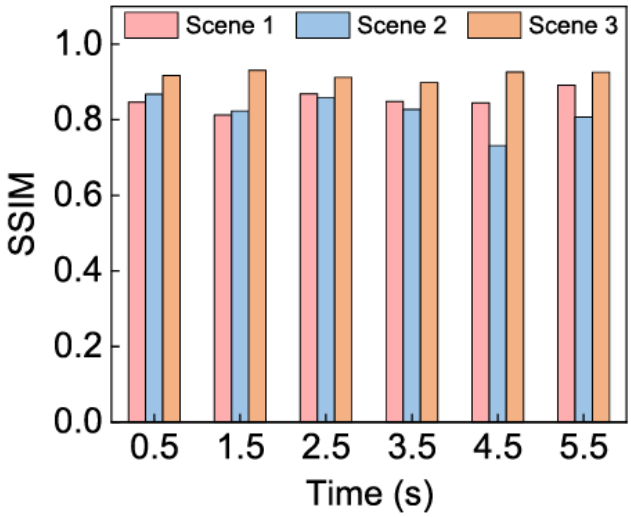

Figure S17. The SSIM result of three scenes for different prediction time.

Table S1. Comparison between reported optoelectronic device arrays.

Structure	*Array scale*	*Pixel*	*Active-matrix*	*PPI*	*Function*	*Ref.*
MoS_2	3×3	1PT	-	-	Adaptive Machine Learning and Forgetting	[1]
MoS_2-pV3D3	3×3	1PT	-	-	Image processing	[2]
$PdSe_2/MoTe_2$	3×3	1PT	-	-	Image processing	[3]
$BP/Al_2O_3/WSe_2$	3×3	1PT	-	-	Motion sensing and recognition	[4]
BP	3×3	1PT	-	-	Image processing and recognition	[5]
chlorophyll/PDPP4T	5×5	1PT	-	-	Image processing and recognition	[6]
DTT-8/TFT-CN	5×5	1PT	-	-	motion sensing	[7]
BTBTT6-syn	6×8	1PT	-	-	Image recognition	[8]
PbS/Gr/Pyr-GDY	7×6	1PT	-	-	Optical sensing	[9]
MoS_2	8×8	1PT	-	-	Image processing and recognition	[10]
QD/a-IGZO	10×10	1PT	-	-	Optical sensing	[11]
WSe_2	10×10	1PT	-	-	Color perception, feature extraction, motion sensing	[12]
NbS_2/MoS_2	10×10	1PT	-	-	Image processing, motion sensing	[13]
$CNT/CsPbBr_3$	16×16	1PT	-	-	Optical sensing	[14]
MoS_2	20×20	1PT	-	-	Motion sensing	[15]
MoS_2	32×32	1PT	-	~81	Image processing and recognition	[16]
Se_xTe_{1-x}	42×42	1PD	-	-	Optical sensing	[17]
IGZO	8×8	2PT	-	-	Image recognition	[18]
DNTT/BHJ	4×4	1PT1C	-	-	Optical sensing	[19]
InGaAs	16×16	1P1R	-	-	Image processing	[20]
InGaAs	16×16	1P1R	-	-	Image processing and recognition	[21]
IGZO/CdS	7×7	1PT1T1R	-	~23	Image recognition	[22]
WS_2	6×6	1T1PT	-	-	Optical sensing	[23]
IGZO/CdSe/CdSe/CdS	12×12	1T1PT	√	~42	Optical sensing	[24]
In_2O_3/PTB7-Th: BTPV-4F	16×16	1T1PT	√	40	Optical sensing, Image processing	[25]
In_2O_3/BHJ	32×64	1T1PT	√	128	Optical sensing	[26]
Monolayer MoS_2	**64×64**	**1T1PD**	√	**163**	**Image processing, motion sensing and predicting**	**This work**

Table S2. **The statistics for the Ln-IZO TFTs.**

	μ_{sat} (cm^{-2} V^{-1} s^{-1})	lg(I_{on}/I_{off})	V_{th} (V)	SS (V dec^{-1})
Mean	8.04	10.05	-1.43	0.16
Standard Deviation	0.31	0.48	0.34	0.07
Median	8.18	9.95	-1.42	0.15

Supporting References

[1] A. Dodda, D. Jayachandran, S. Subbulakshmi Radhakrishnan, A. Pannone, Y. Zhang, N. Trainor, J. M. Redwing, S. Das, *ACS Nano* **2022**, 16, 20010.

[2] C. Choi, J. Leem, M. Kim, A. Taqieddin, C. Cho, K. W. Cho, G. J. Lee, H. Seung, H. J. Bae, Y. M. Song, T. Hyeon, N. R. Aluru, S. Nam, D. H. Kim, *Nat. Commun.* **2020**, 11, 5934.

[3] L. Pi, P. Wang, S.-J. Liang, P. Luo, H. Wang, D. Li, Z. Li, P. Chen, X. Zhou, F. Miao, T. Zhai, *Nat. Electron.* **2022**, 5, 248.

[4] Z. Zhang, S. Wang, C. Liu, R. Xie, W. Hu, P. Zhou, *Nat. Nanotechnol.* **2022**, 17, 27.

[5] S. Lee, R. Peng, C. Wu, M. Li, *Nat. Commun.* **2022**, 13, 1485.

[6] B. Yang, Y. Lu, D. Jiang, Z. Li, Y. Zeng, S. Zhang, Y. Ye, Z. Liu, Q. Ou, Y. Wang, S. Dai, Y. Yi, J. Huang, *Adv. Mater.* **2020**, 32, 2001227.

[7] X. Zhu, C. Gao, Y. Ren, X. Zhang, E. Li, C. Wang, F. Yang, J. Wu, W. Hu, H. Chen, *Adv. Mater.* **2023**, 35, e2301468.

[8] T. Jiang, Y. Wang, Y. Zheng, L. Wang, X. He, L. Li, Y. Deng, H. Dong, H. Tian, Y. Geng, L. Xie, Y. Lei, H. Ling, D. Ji, W. Hu, *Nat. Commun.* **2023**, 14, 2281.

[9] Y. X. Hou, Y. Li, Z. C. Zhang, J. Q. Li, D. H. Qi, X. D. Chen, J. J. Wang, B. W. Yao, M. X. Yu, T. B. Lu, J. Zhang, *ACS Nano* **2021**, 15, 1497.

[10] F. Liao, Z. Zhou, B. J. Kim, J. Chen, J. Wang, T. Wan, Y. Zhou, A. T. Hoang, C. Wang, J. Kang, J.-H. Ahn, Y. Chai, *Nat. Electron.* **2022**, 5, 84.

[11] J. Kim, S.-M. Kwon, Y. K. Kang, Y.-H. Kim, M.-J. Lee, K. Han, A. Facchetti, M.-G. Kim, S. K. Park, *Sci. Adv.* **2019**, 5, eaax8801.

[12] Z. Peng, L. Tong, W. Shi, L. Xu, X. Huang, Z. Li, X. Yu, X. Meng, X. He, S. Lv, G. Yang, H. Hao, T. Jiang, X. Miao, L. Ye, *Nat. Commun.* **2024**, 15, 8650.

[13] P. Y. Huang, B. Y. Jiang, H. J. Chen, J. Y. Xu, K. Wang, C. Y. Zhu, X. Y. Hu, D. Li, L. Zhen, F. C. Zhou, J. K. Qin, C. Y. Xu, *Nat. Commun.* **2023**, 14, 6736.

[14] Q. B. Zhu, B. Li, D. D. Yang, C. Liu, S. Feng, M. L. Chen, Y. Sun, Y. N. Tian, X. Su, X. M. Wang, S. Qiu, Q. W. Li, X. M. Li, H. B. Zeng, H. M. Cheng, D. M. Sun, *Nat. Commun.* **2021**, 12, 1798.

[15] J. Chen, Z. Zhou, B. J. Kim, Y. Zhou, Z. Wang, T. Wan, J. Yan, J. Kang, J. H. Ahn, Y. Chai, *Nat. Nanotechnol.* **2023**, 18, 882.

[16] H. Jang, C. Liu, H. Hinton, M. H. Lee, H. Kim, M. Seol, H. J. Shin, S. Park, D. Ham, *Adv. Mater.* **2020**, 32, e2002431.

[17] C. Tan, M. Amani, C. Zhao, M. Hettick, X. Song, D. H. Lien, H. Li, M. Yeh, V. R. Shrestha, K. B. Crozier, M. C. Scott, A. Javey, *Adv. Mater.* **2020**, 32, 2001329.

[18] S. Song, C. Choi, J. Ahn, J. J. Lee, J. Jang, B. S. Yu, J. P. Hong, Y. S. Ryu, Y. H. Kim, D. K. Hwang, *InfoMat* **2023**, 5, 12479.

[19] A. Pierre, A. Gaikwad, A. C. Arias, *Nat. Photon.* **2017**, 11, 193.

[20] D. Lee, M. Park, Y. Baek, B. Bae, J. Heo, K. Lee, *Nat. Commun.* **2022**, 13, 5223.

[21] B. Bae, M. Park, D. Lee, I. Sim, K. Lee, *Adv. Optical. Mater.* **2022**, 11, 2201905.

[22] S. M. Kwon, J. Y. Kwak, S. Song, J. Kim, C. Jo, S. S. Cho, S. J. Nam, J. Kim, G. S. Park, Y. H. Kim, S. K. Park, *Adv. Mater.* **2021**, 33, e2105017.

[23] A. Bala, M. Sritharan, N. Liu, M. Naqi, A. Sen, G. Han, H. Y. Rho, Y. Yoon, S. Kim, *InfoMat* **2024**, 6, 12513.

[24] J. Kim, C. Jo, M. G. Kim, G. S. Park, T. J. Marks, A. Facchetti, S. K. Park, *Adv. Mater.* **2022**, 34, e2106215.

[25] D. Li, Z. Jia, Y. Tang, C. Song, K. Liang, H. Ren, F. Li, Y. Chen, Y. Wang, X. Lu, L. Meng,

B. Zhu, *Nano. Lett.* **2022**, 22, 5434.
[26] D. Li, Y. Chen, H. Ren, Y. Tang, S. Zhang, Y. Wang, L. Xing, Q. Huang, L. Meng, B. Zhu, *Adv. Sci.* **2024**, e2406401.